A SIMULATION OF THE VERTICAL SPLIT HEAD FAILURE IN RAILS

C. H. Kuo and L. M. Keer

Department of Civil Engineering, Northwestern University, 2145 Sheridan Road,
Evanston, IL 60208, U.S.A.

and

R. K. Steele

Technical Center, Association of American Railroads, 3140 South Federal Street,
Chicago, IL 60616, U.S.A.

Abstract—A two-dimensional analysis is presented to assess a possible mechanism to account for the axial cracking behavior in rails which is usually called a vertical split head failure. This failure is potentially damaging and may eventually lead to derailment. The vertical split head is simulated in the present analysis as a vertical crack in an eccentrically loaded infinite strip, representing the head, loaded on its upper surface and constrained on its lower surface, approximating the web constraint. The vertical crack is modeled as distributed dislocations. By using Fourier tarnsforms, the interior stress field and stress intensity factors at the crack tip are determined from the derived coupled integral equations. The calculated stress field indicates that the initiation of a vertical defect is more likely to be caused by the influence of residual stresses upon an existing rail defect, such as an inclusion. Moreover, the growth of the crack is constrained to within the rail head by the high magnitudes of compressive stresses that occur beneath the contact loading and the head-web juncture.

1. INTRODUCTION

Contact fatigue failure that is caused by repeated wheel passages is known to be a common cause of derailment accidents. The fatigue cracks generally initiate within the rail head and will propagate further either along the rail (longitudinal defects) or across the rail head (transverse defects), as the defects are subjected to subsequent wheel/rail contacts. A serious failure belonging to the class of longitudinal internal defects is the vertical split head failure (VSH), which is vertically oriented with the crack surface parallel to the rail [see Fig. 1(a)]. A complete fracture from the VSH can result in the loss of substantial length of running surface (Mayville, 1985). Contact fatigue analysis is essential to the determination of significant parameters leading to fatigue failure, such as the critical flaw size and the rate with which the defects grow.

Many research efforts have been contributed to the study of the transverse defects [see e.g. Hearle and Johnson (1985) and Sheppard *et al.* (1985)]. As the initial defects that develop in the rail are near the wheel/rail contact area, which has dimensions smaller than the overall rail size, the transverse defects are generally treated as a subsurface crack in a semi-infinie body by ignoring the effect from bottom surface of the rail head. Farris *et al.* (1987) presented a two-dimensional cracking model combined with stability analysis of a fatigue crack path to study the possible mechanism involved with a shell defect that becomes unstable and turns into a transverse defect (detail fracture). For the vertical defects that develop in the rail head, the web and rail bases, due to their stiffness and fracture toughness, could prevent the crack from running into the rail web. As the defects are subjected to repeated wheel contacts, the crack may continue to grow longitudinally along the rail and eventually leads to a vertical split head. Although the VSH, because of possible loss of guidance of the wheel, is considered dangerous, its fracture mechanisms are still not quite clear. The purpose of this paper is to present a two-dimensional plane strain model to estimate the propagation behavior of the VSH from the standpoint of linear elastic contact and fracture analysis, assuming that a relatively long longitudinal crack has already been developed.
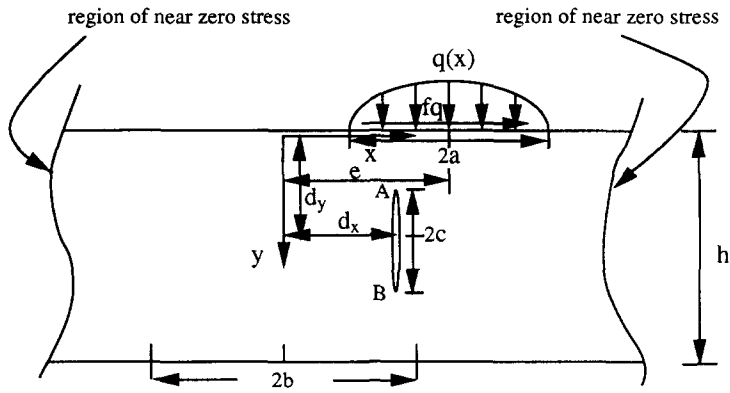
Fig. 1(b). Problem configuration: cross-sectional representation of rail.

In the present paper, the VSH is idealized as a vertical crack in the infinitely wide strip (assuming that edge effects are negligible), which is fixed on a portion of the bottom surface by juncture with the web and loaded by an eccentric Hertzian contact at the top surface. The plane strain assumption assumes that the crack is infinitely long in the longitudinal direction. In Section 2, the vertical crack is modeled as a group of edge dislocations distributed along the crack surface. The contact and crack problems are analysed by the Fourier transform, which reduces the problems to the coupled integral equations which have Cauchy singular kernels, the details of which are included in the Appendices. The numerical procedure for solving the Cauchy singular integral equations is described briefly in Section 3. The technique developed by Miller and Keer (1985) is used to generate a set of quadrature formulae, which reduce the integral equations into a set of algebraic equations. Numerical results for the physical consideration of the VSH are discussed in Section 4. The interior stress distributions due to eccentric contact loading are shown in terms of maximum principal stress and von Mises stress. The significant parameters associated with the VSH such as the eccentricity of wheel loading, crack size and presumed residual stresses are examined on the basis of the calculated stress intensity factors.

2. MATHEMATICAL FORMULATION

A two-dimensional model is shown in Fig. 1(b), which models the cross-section of the rail of Fig. 1(a) with an existing vertical crack loaded by eccentric wheel contact. Since the contact region is generally relatively small compared with the width of the rail head, the strip is idealized as infinite in extent in the transverse direction with height, h. To consider the influence of the head-web fillet, the approximate fixed boundary conditions is prescribed along the head-web fillet, $-b \leqslant x \leqslant b$, $y = h$, together with the free traction condition on the remaining portions. Hertzian contact loading is applied on the rail surface with eccentricity of e, contact length a. A crack of length $2c$ is located at a distance d_x from the centerline of the rail and d_y below the rail surface. As previously mentioned the length of the crack in the longitudinal direction is assumed sufficiently large that the model can be treated as a plane strain problem.

At first the contact problem in the absence of the vertical crack is considered. The boundary conditions for the contact problem can be described as follows:

$$\sigma_{yy}(x, 0) = -\frac{P_N}{2\pi a} \sqrt{1 - \frac{(x-e)^2}{a^2}}, \quad |x-e| \leqslant a, y = 0, \tag{1}$$

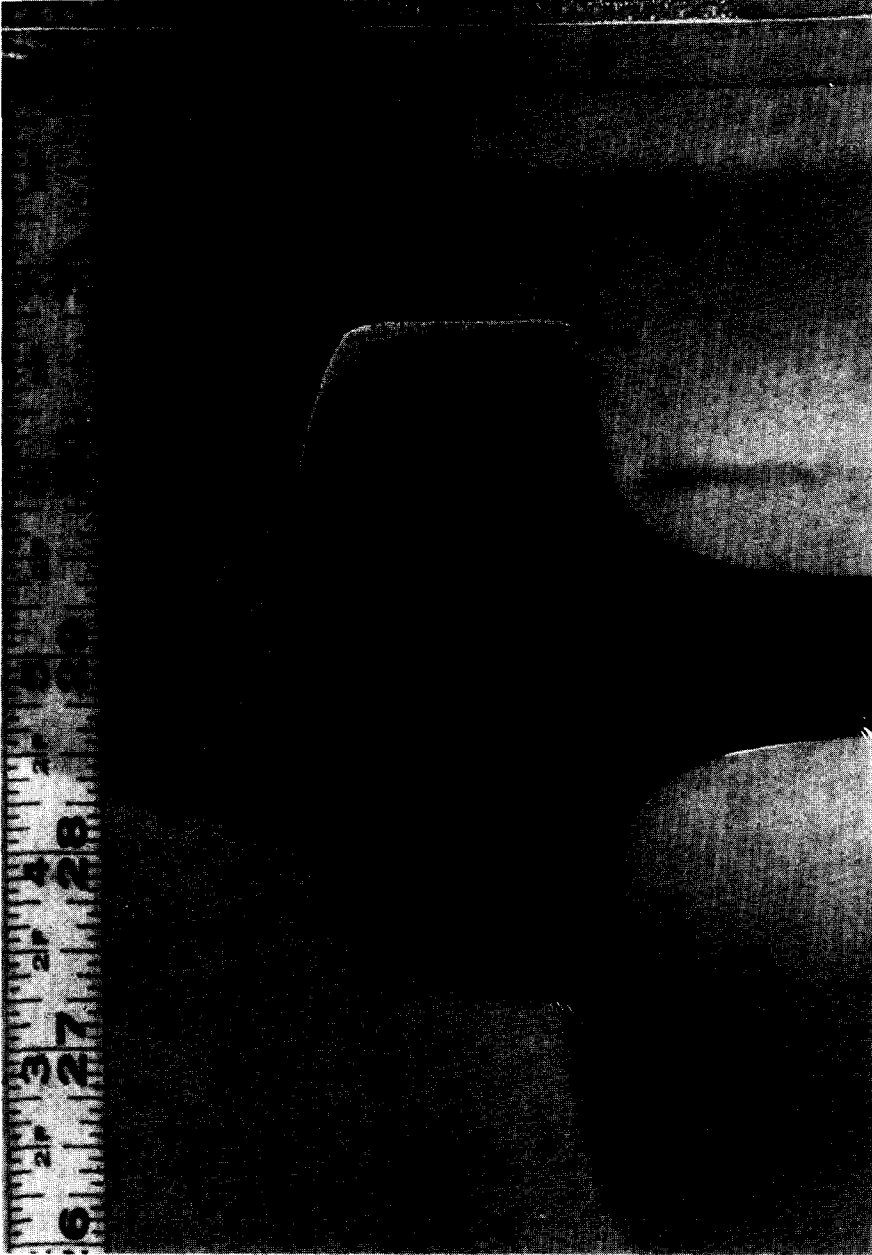$$\sigma_{yx}(x, 0) = -\frac{fP_N}{2\pi a} \sqrt{1 - \frac{(x-e)^2}{a^2}}, \quad |x-e| \leqslant a, y = 0, \tag{2}$$

Fig. 1(a). Photograph depicting cross-section of rail with vertical split head.

$$\sigma_{yy}(x,0) = \sigma_{yx}(x,0) = 0, \quad |x-e| > a, \, y = 0, \tag{3}$$

$$\frac{\partial u_y(x,h)}{\partial x} = \frac{\partial u_x(x,h)}{\partial x} = 0, \quad |x| \leqslant b, \, y = h, \tag{4}$$

$$\sigma_{yy}(x,h) = \sigma_{yx}(x,h) = 0, \quad |x| > b, \, y = h, \tag{5}$$

where P_N is the total load applied on the rail and f is the coefficient of contact friction between wheel and rail surface. Equation (2) assumed that traction is from limiting friction $\tau = \mu\sigma$ and is purely longitudinal. Here it is assumed that the stress disribution is Hertzian and will not be affected either by the layer thickness or by the edge effects.

To solve the two-dimensional problem, the displacement and stress fields are expressed in terms of the Papkovich–Neuber potentials, which give

$$2\mu\mu_x = -y\frac{\partial\Phi}{\partial x} - \frac{\partial\Psi}{\partial x}, \tag{6}$$

$$2\mu\mu_y = \kappa\Phi - y\frac{\partial\Phi}{\partial y} - \frac{\partial\Psi}{\partial y}, \tag{7}$$

$$\sigma_{xx} = \tfrac{1}{2}(3-\kappa)\frac{\partial\Phi}{\partial y} - \left(y\frac{\partial^2\Phi}{\partial x^2} + \frac{\partial^2\Psi}{\partial x^2}\right), \tag{8}$$

$$\sigma_{xy} = \tfrac{1}{2}(\kappa-1)\frac{\partial\Phi}{\partial x} - \left(y\frac{\partial^2\Phi}{\partial x\,\partial y} + \frac{\partial^2\Psi}{\partial x\,\partial y}\right), \tag{9}$$

$$\sigma_{yy} = \tfrac{1}{2}(\kappa+1)\frac{\partial\Phi}{\partial y} - \left(y\frac{\partial^2\Phi}{\partial y^2} + \frac{\partial^2\Psi}{\partial y^2}\right), \tag{10}$$

where $\kappa = 3-4v$ for plane strain, $\kappa = (3-v)/(1+v)$ for generalized plane stress and v is Poisson's ratio. The functions Φ and Ψ satisfy Laplace's equation. The general solutions for the potential functions in the strip, $0 \leqslant y \leqslant h$, can be expressed by the Fourier transform:

$$\Phi(x,y) = \frac{1}{2\pi}\int_{-\infty}^{\infty} (A(\eta)\,e^{-\eta y} + B(\eta)\,e^{\eta(y-h)})\,e^{i\eta x}\,d\eta/\eta, \tag{11}$$

$$\Psi(x,y) = \frac{1}{2\pi}\int_{-\infty}^{\infty} (C(\eta)\,e^{-\eta y} + D(\eta)\,e^{\eta(y-h)})\,e^{i\eta x}\,d\eta/\eta. \tag{12}$$

To solve this mixed boundary value problem the unknown functions, $A(\eta)$, $B(\eta)$, $C(\eta)$ and $D(\eta)$ that satisfy the prescribed boundary conditions (1)–(5) must be solved. From eqns (6)–(12), the unknown functions in the transformed domain can be expressed as

$$T_i = D_{ij}^{-1}S_j, \tag{13}$$

where

$$\mathbf{T} = \begin{Bmatrix} A \\ C \\ B \\ D \end{Bmatrix}, \tag{14}$$

$$\mathbf{D} = \begin{bmatrix} \dfrac{i(\kappa-1)}{2} & i|\eta| & \dfrac{i(\kappa-1)}{2}\,\mathrm{e}^{-\eta h} & -i|\eta|\,\mathrm{e}^{-\eta h} \\[2ex] -\dfrac{(\kappa+1)|\eta|}{2\eta} & -\eta & \dfrac{(\kappa+1)|\eta|}{2\eta}\,\mathrm{e}^{-\eta h} & -\eta\,\mathrm{e}^{-\eta h} \\[2ex] i\left[\dfrac{(\kappa-1)}{2}+h|\eta|\right]\mathrm{e}^{-\eta h} & i|\eta|\,\mathrm{e}^{-\eta h} & i\left[\dfrac{(\kappa-1)}{2}-h|\eta|\right] & -i|\eta| \\[2ex] \left[-\dfrac{(\kappa+1)|\eta|}{2\eta}-h|\eta|\right]\mathrm{e}^{-\eta h} & -\eta\,\mathrm{e}^{-\eta h} & \left[\dfrac{(\kappa+1)|\eta|}{2\eta}-h|\eta|\right] & \eta \end{bmatrix}, \tag{15}$$

$$\mathbf{S} = \begin{Bmatrix} S_{xy}(0) \\ S_{yy}(0) \\ S_{xy}(h) \\ S_{yy}(h) \end{Bmatrix}. \tag{16}$$

The vector S represents the transformed components of the applied stresses on the top and bottom surfaces of the strip.

In order to calculate the stress fields in the strip, first the traction distributed along the fixed region must be determined. By eliminating the unknown functions and introducing the boundary conditions, a set of coupled singular integral equations are obtained as,

$$\int_{-b}^{b}\left[\frac{\kappa+1}{2(t-x)}+k_{11}(x,t)\right]t_x(t)\,\mathrm{d}t + \frac{\pi(\kappa-1)}{2}\,t_y(x) + \int_{-b}^{b}k_{12}(x,t)t_y(t)\,\mathrm{d}t = p_1, \quad -b \leqslant x \leqslant b, \tag{17}$$

$$-\frac{\pi(\kappa-1)}{2}\,t_x(x) + \int_{-b}^{b}k_{21}(x,t)t_x(t)\,\mathrm{d}t + \int_{-b}^{b}\left[\frac{\kappa+1}{2(t-x)}+k_{22}(x,t)\right]t_y(t)\,\mathrm{d}t = p_2, \quad -b \leqslant x \leqslant b, \tag{18}$$

where

$$k_{11} = \int_0^{\infty}\frac{(\kappa+1)\,\mathrm{e}^{-2h\eta}\,(1-2h\eta+2h^2\eta^2-\mathrm{e}^{-2h\eta})\sin\eta(x-t)}{\Delta}\,\mathrm{d}\eta, \tag{19}$$

$$k_{12} = -k_{21} = \int_0^{\infty}\frac{-2(\kappa+1)h^2\eta^2\,\mathrm{e}^{-2h\eta}\cos\eta(x-t)}{\Delta}\,\mathrm{d}\eta, \tag{20}$$

$$k_{22} = \int_0^{\infty}\frac{(\kappa+1)\,\mathrm{e}^{-2h\eta}\,(1+2h\eta+2h^2\eta^2-\mathrm{e}^{-2h\eta})\sin\eta(x-t)}{\Delta}\,\mathrm{d}\eta, \tag{21}$$

$$p_1 = \frac{2P}{a}\int_0^{\infty}\frac{(\kappa+1)J_1(\eta a)\,\mathrm{e}^{-h\eta}}{\eta\Delta}\,[-f(1-h\eta-\mathrm{e}^{-2h\eta}-h\eta\,\mathrm{e}^{-2h\eta})\sin\eta(x-e)$$

$$+h\eta(1-\mathrm{e}^{-2h\eta})\cos\eta(x-e)]\,\mathrm{d}\eta, \tag{22}$$

$$p_2 = \frac{2P}{a} \int_0^\infty \frac{(\kappa+1)J_1(\eta a)\,e^{-h\eta}}{\eta\Delta} [fh\eta(1-e^{-2h\eta})\cos\eta(x-e)$$

$$-(1+h\eta-e^{-2h\eta}+h\eta\,e^{-2h\eta})\sin\eta(x-e)]\,d\eta, \quad (23)$$

$$\Delta = -1+2\,e^{-2h\eta}+4h^2\eta^2\,e^{-2h\eta}-e^{-4h\eta}. \quad (24)$$

Equations (17) and (18) are coupled Cauchy singular integral equations of the second kind. The unknown functions $t_x(x)$ and $t_y(x)$ represent the traction distributed over the region, $-b \leqslant x \leqslant b$, required to satisfy the fixed boundary conditions. It is noted that the regular kernels, k_{12} and k_{22}, are not convergent at the lower limits of the integration, as $\eta \to 0$. The divergence of the kernels can be eliminated by the equilibrium conditions:

$$\int_{-b}^{b} t_x(t)\,dt = fP_N, \quad (25)$$

$$\int_{-b}^{b} t_y(t)\,dt = P_N, \quad (26)$$

and

$$\frac{2P_N}{\pi a}\int_{-a}^{a}\sqrt{1-\frac{(t-e)^2}{a^2}}\,t\,dt + \int_{-b}^{b} t_y(t)t\,dt$$

$$+\frac{h}{2}\left[\frac{2fP_N}{\pi a}\int_{-a}^{a}\sqrt{1-\frac{(t-e)^2}{a^2}}\,t\,dt - \int_{-b}^{b} t_x(t)t\,dt\right] = 0. \quad (27)$$

With the solved tractions precribed along the fixed region, the elastic fields in the transformed domain can be obtained from transformed components of applied stresses on both boundaries. The stress components are obtained by inversion of the Fourier transforms as

$$\sigma_{xx} = \sigma_{xx}^{H} + \sigma_{xx}^{P} + \frac{1}{\pi}\int_0^\infty \left[b_{11}\frac{f\pi}{\eta}J_1(\eta a)\sin\eta(x-e) - b_{12}\frac{\pi}{\eta}J_1(\eta a)\cos\eta(x-e)\right.$$

$$\left. - b_{13}\int_{-b}^{b} t_x(t)\sin\eta(x-t)\,dt + b_{14}\int_{-b}^{b} t_y(t)\cos\eta(x-t)\,dt\right]d\eta, \quad (28)$$

$$\sigma_{yy} = \sigma_{yy}^{H} + \sigma_{yy}^{P} + \frac{1}{\pi}\int_0^\infty \left[b_{21}\frac{f\pi}{\eta}J_1(\eta a)\sin\eta(x-e) - b_{22}\frac{\pi}{\eta}J_1(\eta a)\cos\eta(x-e)\right.$$

$$\left. - b_{23}\int_{-b}^{b} t_x(t)\sin\eta(x-t)\,dt + b_{24}\int_{-b}^{b} t_y(t)\cos\eta(x-t)\,dt\right]d\eta, \quad (29)$$

$$\sigma_{xy} = \sigma_{xy}^{H} + \sigma_{xy}^{P} + \frac{1}{\pi}\int_0^\infty \left[-b_{31}\frac{f\pi}{\eta}J_1(\eta a)\cos\eta(x-e) + b_{32}\frac{\pi}{\eta}J_1(\eta a)\sin\eta(x-e)\right.$$

$$\left. + b_{33}\int_{-b}^{b} t_x(t)\cos\eta(x-t)\,dt - b_{34}\int_{-b}^{b} t_y(t)\sin\eta(x-t)\,dt\right]d\eta. \quad (30)$$

The superscripts H and P respectively correspond to the stress fields due to the Hertzian contact loading and the distributed traction applied to the half-plane. The symbols b_{ij}, $i = 1, 3, j = 1, 4$, in eqns (28)–(30) are defined in Appendix A.

    Consider next the contact problem of an existing vertical crack in the infinite strip, which is loaded by Hertzian contact. The center of crack is located at $x = d_x$, $y = d_y$ with

length $2c$. As the crack surface could experience complicated contact stresses, the crack may be considered to be partially or fully closed. Thus, the boundary conditions along the crack surface can be described as:

$$\sigma_{xy} = 0, \quad |y - d_y| \leqslant c, x = d_x, \tag{31}$$

$$\sigma_{xx} = 0, \quad y \in C - C^*, x = d_x, \tag{32}$$

$$\frac{\partial u_x(d_x^+, t)}{\partial y} - \frac{\partial u_x(d_x^+, t)}{\partial y} = 0, \quad y \in C^*, x = d_x. \tag{33}$$

The closed portion of the crack, denoted by C^*, is assumed to be in frictionless contact with normal tractions transmitted between the crack surface. Although there will be friction on the crack surfaces, they are assumed to be small relative to the other stresses. To analyse the crack problem, the crack is modeled as distributed edge dislocations along the crack surface. In an infinite plane, the single edge dislocation at $x = d_x$, $y = t$ is defined by

$$\frac{\partial u_x(d_x^+, t)}{\partial y} - \frac{\partial u_x(d_x^+, t)}{\partial y} = -b_x \delta(y - t), \tag{34}$$

$$\frac{\partial u_y(d_x^+, t)}{\partial y} - \frac{\partial u_y(d_x^+, t)}{\partial y} = -b_y \delta(y - t), \tag{35}$$

where b_x and b_y are the dislocation densities. For the contact problem including the distributed dislocations, the elastic fields in the strip can be obtained by superposing appropriate components as in the following expression:

$$\frac{\partial u_i^T}{\partial x} = \frac{\partial u_i^C}{\partial x} - \frac{\partial u_i^D}{\partial x} + \frac{\partial u_i^F}{\partial x} \tag{36}$$

and

$$\sigma_{ij}^T = \sigma_{ij}^C - \sigma_{ij}^D + \sigma_{ij}^F, \tag{37}$$

"T"   the total elastic fields,
"C"   the Hertzian contact without the defect,
"D"   the equivalent stresses due to the distributed dislocations applied on both surfaces of the strip,
"F"   the distributed dislocations in an infinite plane.

The elastic fields due to the distributed dislocations in an infinite plane are listed in Appendix B. Therefore, by imposing the boundary conditions along the fixed boundary and the crack surface, the integral equations can be derived as

$$\frac{\kappa+1}{2} \int_{-b}^{b} \frac{1}{t-x} t_x(t) \, dt + \frac{\pi(\kappa-1)}{2} t_y(x) + \int_{-b}^{b} [k_{11}(x, h, t) t_x(t) + k_{12}(x, h, t) t_y(t)] \, dt$$

$$+ \int_{d_y-c}^{d_y+c} [k_{13}(x, h, t) b_x(t) + k_{14}(x, h, t) b_y(t)] \, dt = p_1, \quad -b \leqslant x \leqslant b, y = h, \tag{38}$$

$$-\frac{\pi(\kappa-1)}{2} t_x(x) + \frac{\kappa+1}{2} \int_{-b}^{b} \frac{1}{t-x} t_y(t) \, dt + \int_{-b}^{b} [k_{21}(x, h, t) t_x(t) + k_{22}(x, h, t) t_y(t)] \, dt$$

$$+ \int_{d_y-c}^{d_y+c} [k_{23}(x, h, t) b_x(t) + k_{24}(x, h, t) b_y(t)] \, dt = p_2, \quad -b \leqslant x \leqslant b, y = h, \tag{39}$$

$$\frac{-2\mu}{\kappa+1}\int_{d_y-c}^{d_y+c}\frac{1}{t-y}b_x(t)\,\mathrm{d}t+\int_{-b}^{b}[k_{31}(d_x,y,t)t_x(t)+k_{32}(d_x,y,t)t_y(t)]\,\mathrm{d}t$$

$$+\int_{d_y-c}^{d_y+c}k_{33}(d_x,y,t)b_x(t)\,\mathrm{d}t=p_3,\quad d_y-c\leqslant y\leqslant d_y+c,\,x=d_x,\quad(40)$$

$$\frac{-2\mu}{\kappa+1}\int_{d_y-c}^{d_y+c}\frac{1}{t-y}b_y(t)\,\mathrm{d}t+\int_{-b}^{b}[k_{41}(d_x,y,t)t_x(t)+k_{42}(d_x,y,t)t_y(t)]\,\mathrm{d}t$$

$$+\int_{d_y-c}^{d_y+c}k_{44}(d_x,y,t)b_y(t)\,\mathrm{d}t=p_4,\quad d_y-c\leqslant y\leqslant d_y+c,\,x=d_x.\quad(41)$$

The kernels k_{ij}, $i,j=1,4$ and external forces p_i, $i=1,4$ are given in Appendix C. The kernels k_{13}, k_{14}, k_{23}, k_{24}, k_{31}, k_{32}, k_{41} and k_{42} represent the interaction between the crack and the fixed boundary. The crack opening displacements at a point $y=s$ can be obtained from

$$\Delta u_x=-\int_{d_y-c}^{s}b_x(t)\,\mathrm{d}t,\quad(42)$$

$$\Delta u_y=-\int_{d_y-c}^{s}b_y(t)\,\mathrm{d}t\quad(43)$$

and Mode I and II stress intensity factors at the crack tip can be defined as

$$K_{\mathrm{I}}=\frac{2\mu}{1+\kappa}\lim_{y\to d_y+c}\sqrt{c^2-(y-d_y)^2}\,b_x(y),\quad(44)$$

$$K_{\mathrm{II}}=\frac{2\mu}{1+\kappa}\lim_{y\to d_y+c}\sqrt{c^2-(y-d_y)^2}\,b_y(y).\quad(45)$$

3. NUMERICAL ANALYSIS

Equations (17), (18) and (38)–(41) are two systems of coupled Fredholm integral equations of the second kind with a Cauchy singular kernel. Cauchy singular integral equations have been considered in general by Muskhelishvili (1953) and the numerical methods for solving such equations were summarized by Erdogan et al. (1973). Since eqns (38)–(41) can be considered as the general case of eqns (17) and (18), the numerical procedure to solve the integral equations (38)–(41) is described as follows. First, the equations are further simplified by combining them as

$$\frac{\kappa+1}{2}\int_{-b}^{b}\frac{T(t)}{t-x}\,\mathrm{d}t+\frac{(\kappa-1)}{2i}T(x)+\int_{-b}^{b}[K_{11}(x,h,t)T(t)+K_{12}(x,h,t)\bar{T}(t)]\,\mathrm{d}t$$

$$+\int_{d_y-c}^{d_y+c}[K_{13}(x,h,t)B(t)+K_{14}(x,h,t)\bar{B}(t)]\,\mathrm{d}t=P_1,\quad-b\leqslant x\leqslant b,\,y=h,\quad(46)$$

$$\frac{-2\mu}{\lambda+1}\int_{d_y-c}^{d_y+c}\frac{B(t)}{t-y}\,\mathrm{d}t+\int_{-b}^{b}[K_{21}(d_x,y,t)T(t)+K_{22}(d_x,y,t)\bar{T}(t)]\,\mathrm{d}t$$

$$+\int_{d_y-c}^{d_y+c}[K_{23}(d_x,y,t)B(t)+K_{24}(d_x,y,t)\bar{B}(t)]\,\mathrm{d}t=P_2,\quad x=d_x,\,d_y-c\leqslant y\leqslant d_y+c,\quad(47)$$

where

$$T(x) = t_x(x) + it_y(x),$$

$$B(x) = b_x(x) + ib_y(x), \tag{48}$$

$$K_{11} = \tfrac{1}{2}(k_{11} + k_{22}) - ik_{12}, \tag{49}$$

$$K_{12} = \tfrac{1}{2}(k_{11} - k_{22}), \tag{50}$$

$$K_{13} = \tfrac{1}{2}[(k_{13} + k_{24}) - i(k_{14} - k_{23})], \tag{51}$$

$$K_{14} = \tfrac{1}{2}[(k_{13} - k_{24}) + i(k_{14} + k_{23})], \tag{52}$$

$$K_{21} = \tfrac{1}{2}[(k_{31} + k_{42}) - i(k_{32} - k_{41})], \tag{53}$$

$$K_{22} = \tfrac{1}{2}[(k_{31} - k_{42}) + i(k_{32} + k_{41})], \tag{54}$$

$$K_{23} = \tfrac{1}{2}(k_{33} + k_{44}), \tag{55}$$

$$K_{24} = \tfrac{1}{2}(k_{33} - k_{44}), \tag{56}$$

$$P_1 = p_1 + ip_2, \tag{57}$$

$$P_2 = p_3 + ip_4. \tag{58}$$

The integral equations are solved under the assumption that the unknown functions $T(x)$ and $B(x)$ satisfy the Hölder condition on the interval $(-b, b)$. The behavior of the solutions at both end points can be characterized by fundamental functions such that

$$T(x) = \frac{\phi(x)}{(b-x)^\alpha (b+x)^\beta}, \tag{59}$$

$$B(y) = \frac{\varphi(y)}{[c-(y-d_y)]^{1/2}[c+(y-d_y)]^{1/2}}, \tag{60}$$

where

$$\alpha = \frac{1}{2} + \frac{i}{2\pi} \log \kappa, \tag{61}$$

$$\beta = \frac{1}{2} - \frac{i}{2\pi} \log \kappa. \tag{62}$$

In addition, two auxiliary conditions are required to render the solutions unique:

$$\int_{-b}^{b} T(t)\, dt = -fP_N + iP_N, \tag{63}$$

$$\int_{d_y-c}^{d_y+c} B(t)\, dt = 0. \tag{64}$$

Equation (63) represents the overall equilibrium conditions for the applied contact loading and eqn (64) represents the continuity conditions on $x = d_x$ and $|y - d_y| > c$. The solution $T(x)$ has a singularity of an oscillatory type at the end points, while the square root singularity for the solution $B(y)$ is appropriate at the crack tips. The oscillatory singularity arises due to the sharp corner at both ends of the fixed portion, which restricts displacements in the horizontal and vertical directions. The singularity here is also a well-
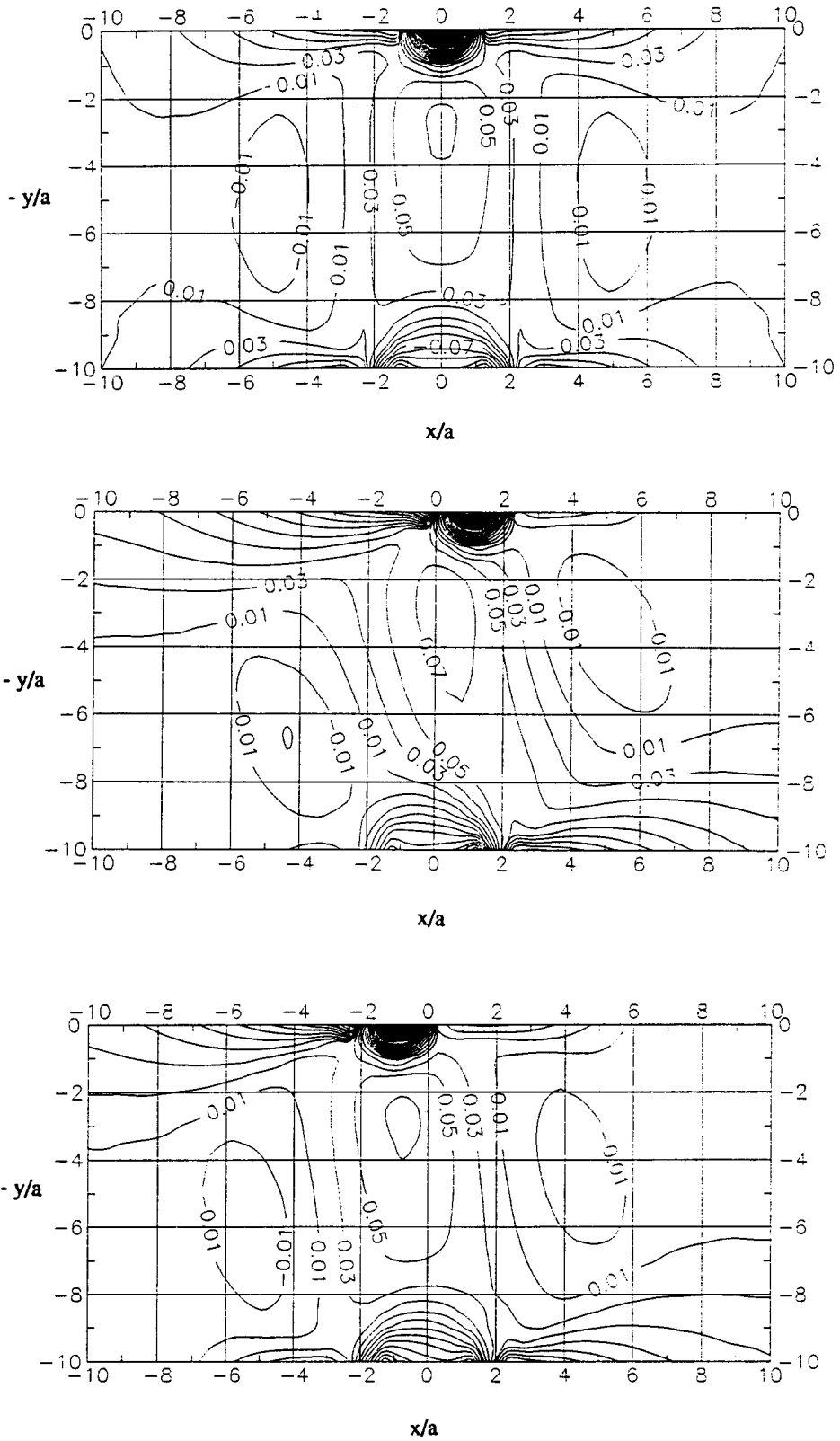
Fig. 2. Contour plots of maximum principal stresses: (a) $f = 0$, $e = 0$, (b) $f = 0.1$, $e = a$, and (c) $f = 0.1$, $e = -a$.
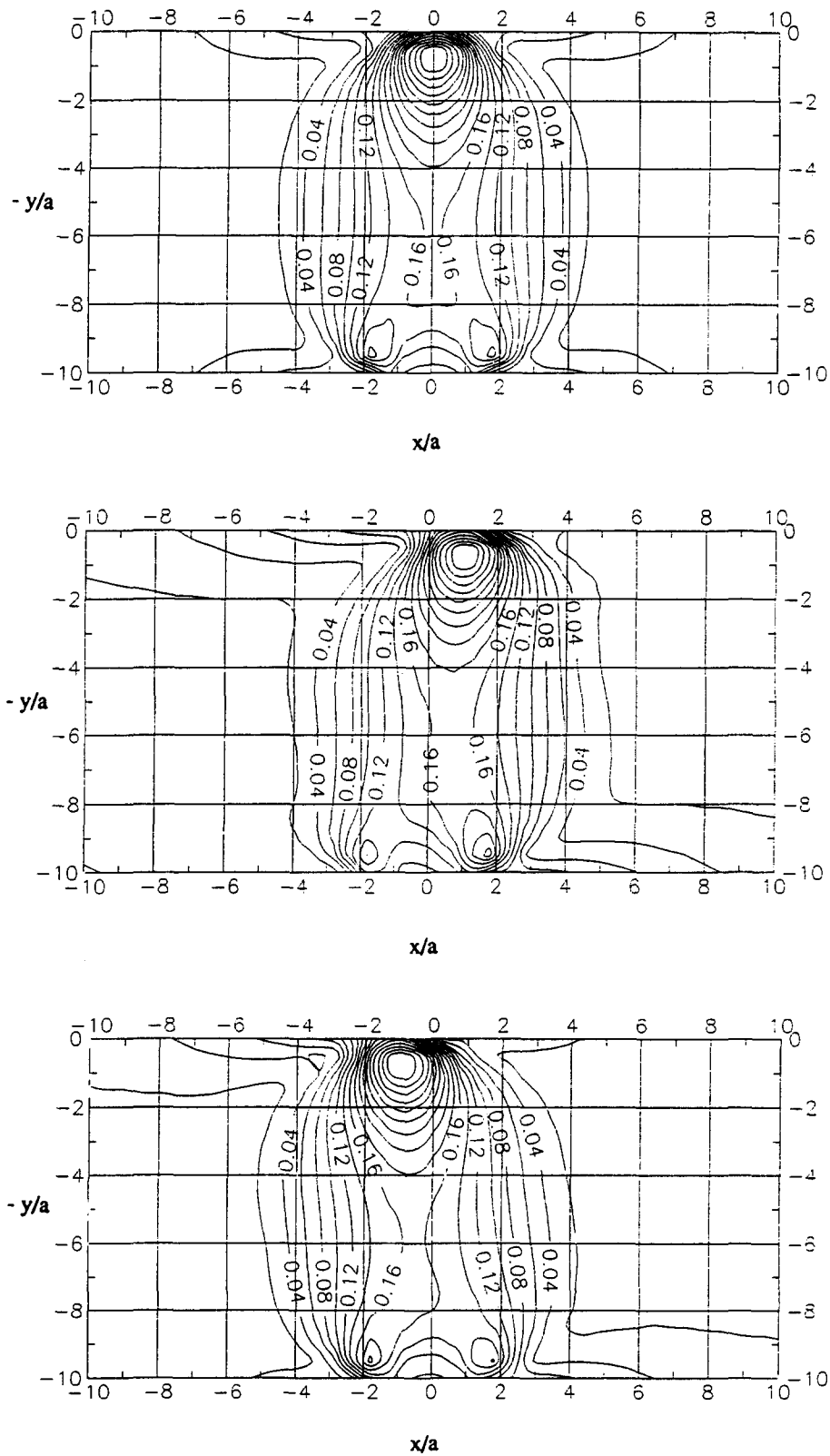
Fig. 3. Contour plots of von Mises stresses: (a) $f = 0$, $e = 0$, (b) $f = 0.1$, $e = a$, and (c) $f = 0.1$, $e = -a$.

known characteristic of the interface crack between dissimilar materials [see e.g. Rice (1988)]. The numerical technique developed by Miller and Keer (1985) is used to solve the integral equations. First, the integration interval is divided into N subintervals, in which the integration points are defined at middle and end points and the collocation points are defined in the middle of two integration points. At each of the subintervals, the kernel function is approximated piecewise by quadratic Lagrange interpolation polynomials and a set of quadrature formulae can be derived. Thus, the integral equations (46) and (47) are reduced to a set of $4N+2$ linear algebraic equations, which can be solved numerically. In general, the number of subintervals, $N = 8$, is adequate to give very accurate solutions.

4. NUMERICAL RESULTS AND DISCUSSION

In the present analysis, physical quantities such as contact loading, contact radius and rail geometries are chosen to represent an actual wheel/rail contact. Assuming that $a/h = 10$, typical parameters for wheel/rail contact are as follows: $a = 4.19$ mm, $h = 41.91$ mm, $b = 7.94$ mm, $P_N = 182.4$ kN, $\mu = 79.565$ GPa, $v = 0.3$ (Orringer et al., 1988).

The interior stress distributions due to an eccentric wheel loading are investigated first. Figures 2(a)–2(c) represent contour plots of the maximum principal stress for different eccentricities of contact loading and friction coefficient. The stress components are normalized to the maximum normal contact stress, q_0. Since the contact loading is concentrated in a relatively small contact area, a high magnitude of compressive stress is localized just beneath the wheel contact region. However, tensile stresses are seen to occur in most of the rail head. The tensile stresses are due primarily to the effects arising from the upper and lower surfaces. It is noted that there exits a submaximum tensile stress near the center of the rail. For the case of $f = e = 0$, the value of submaximum tensile stress is about $0.075q_0$ at $y = 2.5a$ below the contact surface. As is shown in Figs 2(b) and 2(c), the eccentric contact loading and the sliding friction increases the magnitude of tensile stresses, when the direction of the friction is at the same side of contact loading, as shown for example, in Fig. 2(b). Eccentric loading could induce tensile bending stresses near the center of the rail head and frictional contact could cause tensile stresses to arise near the surface at the trailing edge of the contact region. Since the tensile stresses developed in the central region are relatively small, less than 10% of maximum contact stress, the prevailing tensile stresses may not be sufficient to nucleate a vertical defect.

The residual stress as a result of plastic deformation has been recognized as having an important role in the fatigue failure. Figures 3(a)–3(c) are the contour plots of the von
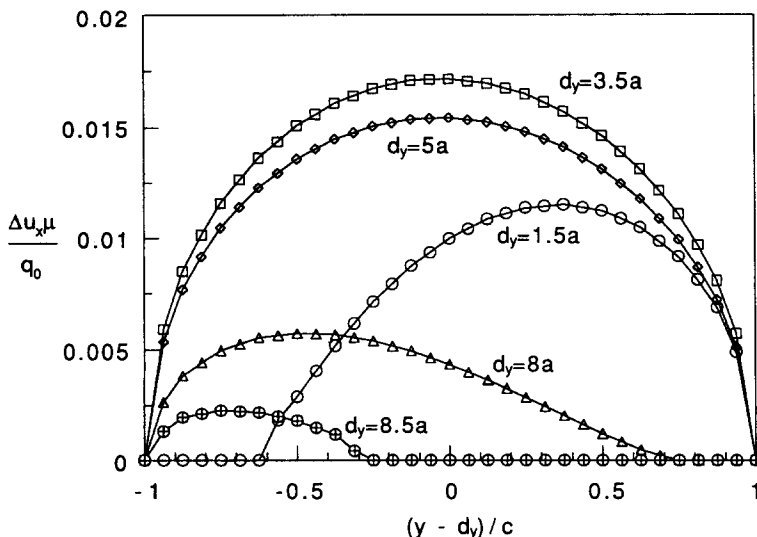

Fig. 4. Crack opening displacements for various locations of the crack with crack length $2c = a$.

Mises stress for different locations of contact loading and friction coefficient. It is noted
that the distribution of von Mises stress near the contact region is very similar to that of
the half-space case. For the case of $f = e = 0$, the maximum von Mises stress is located
approximately at $y = 0.5a$ with a value of $0.36q_0$. Accordingly, plastic deformation may
occur around the region just beneath the contact loading as the von Mises stresses reach
the yield limits. As the plastic deformation is compressive, residual tensile stresses arise in
the stress field.

To study the cracking behavior of the VSH, an existing vertical crack in the infinite
strip is considered. As the crack surface may experience complicated contact stresses, the
crack may be partially or fully closed. Figure 4 shows the crack opening displacements for
the crack with length $2c = a$ at different locations along the y-axis. It is apparent from Fig.
4 that a crack which lies towards the middle of the rail tends to open under the applied
loading, but as a crack tip approaches the top or bottom surfaces of the railhead, that tip
of the crack tends to close. The crack is partially closed as the crack tips approach the top
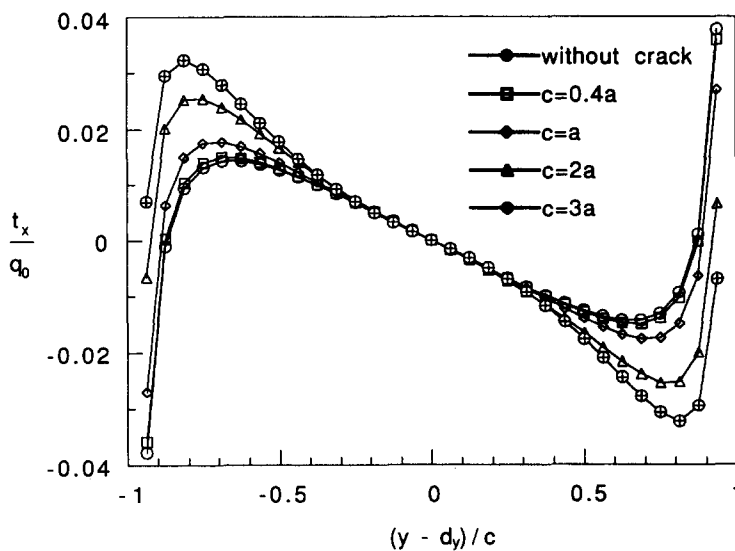

(a)
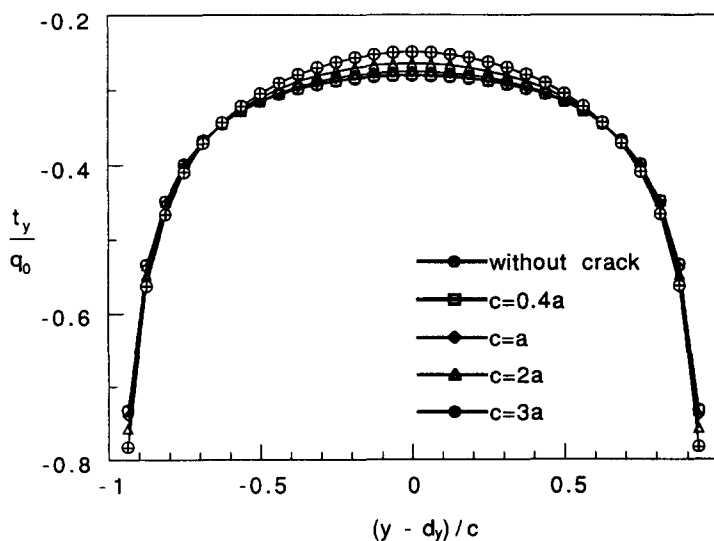
(b)

Fig. 5. Distributed tractions along the fixed boundary for various crack length: (a) tangential
tractions, and (b) normal tractions.

or bottom surfaces. The existence of the defect could interact with the fixed boundary as the lower crack tip approaches the boundary. In Figs 5(a) and 5(b), the distributed tangential and normal tractions along the fixed boundary are shown for various crack lengths and $f = e = 0$. The lower crack tip, point B, is specified on the y-axis at a distance, $d' = 2a$, above the bottom surface. Although the distributions of normal and tangential tractions change slightly with increasing crack length, the effect of the disturbance is insignificant.

As the vertical split head defect is generally observed near the centerline of the rail, in the following discussion a vertical crack will be assumed on the y-axis, $d_x = 0$, with the location of contact stresses varied. Figures 6(a) and 6(b) represent Mode I and II stress intensity factors as a function of location of contact loading. The center of the crack with length $2c = a$ is located at a distance $d_y = 0.3h$ below the top surface and the coefficient of friction is $f = 0.1$. The maximum value of the Mode I stress intensity factor [Fig. 6(a)] exists when the contact loading is applied near the centerline of the rail, i.e. when $e = 0$; accordingly eccentricity of contact loading does not significantly affect Mode I fracture.
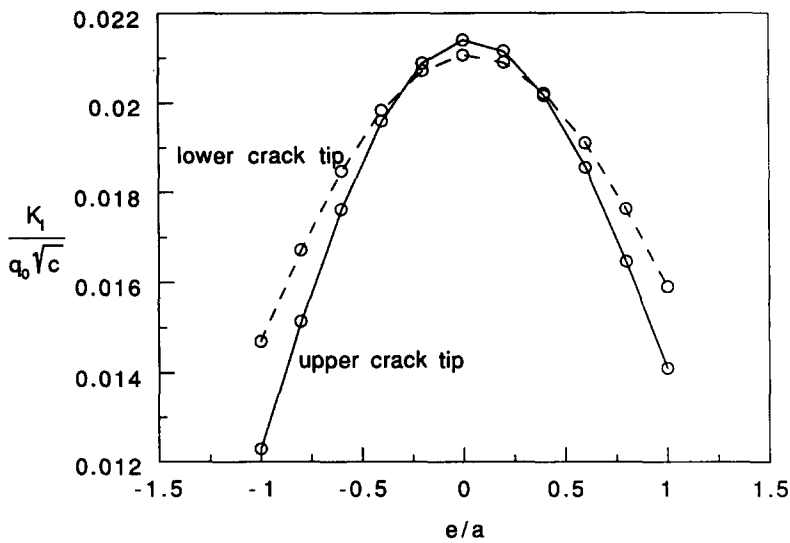
(a)
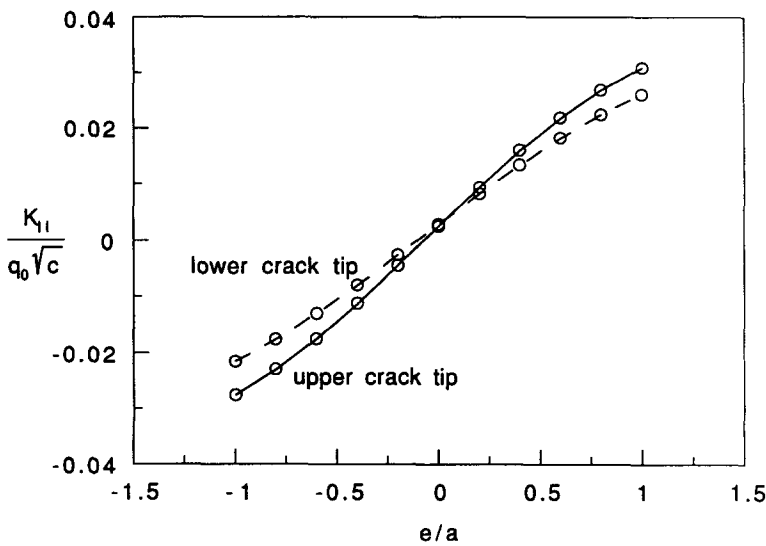
(b)

Fig. 6. Stress intensity factor as a function of location of contact loading ($c = 0.5a$, $f = 0.1$ and $d_x = 0$): (a) K_I, and (b) K_{II}.
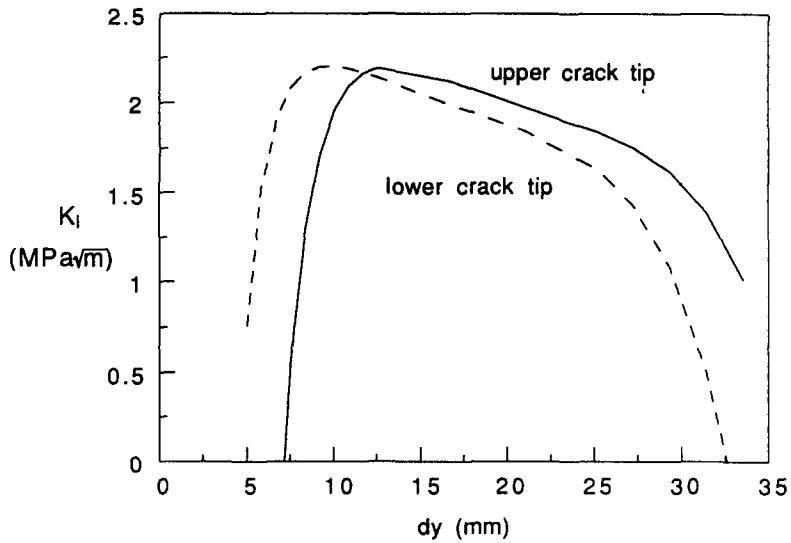
Fig. 7. Mode I stress intensity factor as a function of location of the crack ($c = a$, $f = 0.1$, $e = 0$ and $d_x = 0$).

However, the absolute value of the Mode II stress intensity factor increases with increasing eccentricity of applied loading [Fig. 6(b)].

In general, the fatigue process can be considered as being in two stages: crack initiation and crack propagation. The fracture behavior of standard carbon-steel rails is represented by the threshold stress intensity factor, $\Delta K_{th} = 6.04$ MPa$\sqrt{m}$ and the Paris law: $da/dN = A(\Delta K_I)^n$ where $A = 1.68 \times 10^{-10}$ and $n = 3.3$ (Barsom and Imhof, 1978). Figure 7 shows Mode I stress intensity factors as a function of the locations of the defect along the y-axis with the crack length $2c = 8.38$ mm. The maximum values of stress intensity factors for both crack tips occur approximately at $d_y = 7–13$ mm. The K_I value at the upper crack tip decreases rapidly as the crack approaches the contact region, as does the lower crack tip when it is near the head-web fillet. The stress intensity factor is smaller than the threshold value, ΔK_{th}, required for fatigue crack growth. Therefore, the tensile stresses appear to be
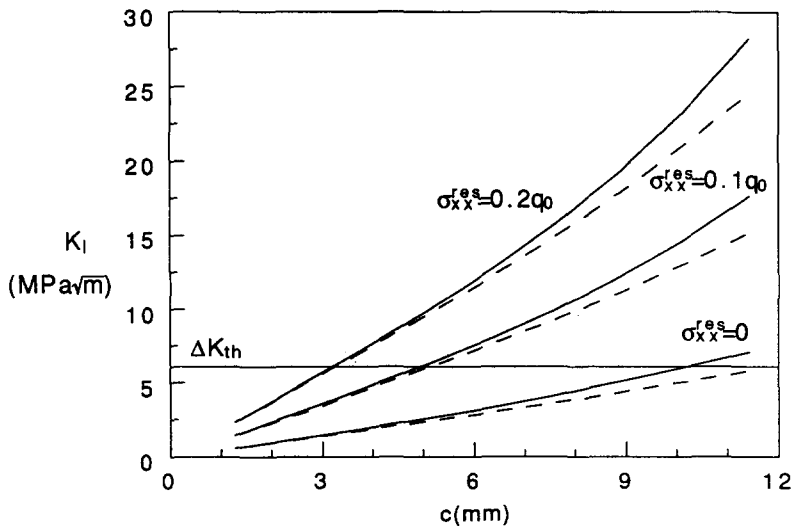

Fig. 8. Mode I stress intensity factror, K_{IA} (solid) and K_{IB} (dash), as a function of crack length for various magnitudes of residual stress ($f = 0.1$, $e = 0$, $d_x = 0$ and $d_y = 17.78$ mm).
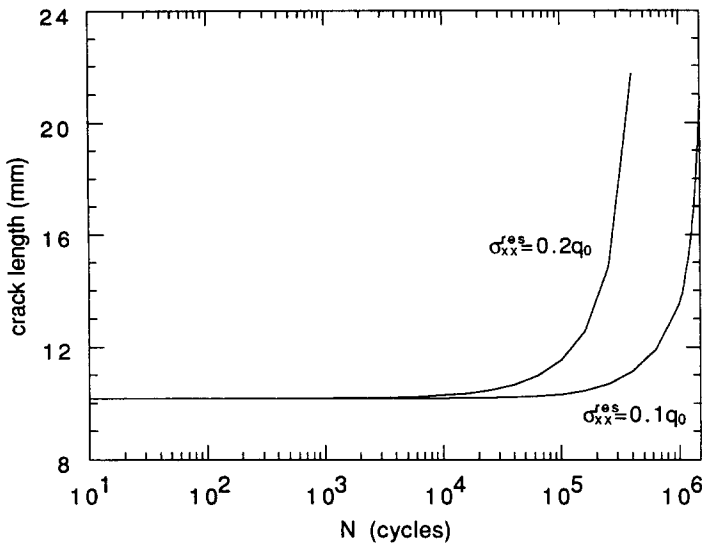
Fig. 9. Crack length as a function of loading cycle for different magnitudes of residual stress ($f = 0.1$, $e = 0$, $d_x = 0$ and $d_y = 17.78$ mm).

insufficient to provide the driving force for further crack growth. From the metallurgical and fracture surface analysis of VSH, the defects generally initiate from the region of inhomogeneous microstructure near the center of the rail head. Miller and Keer (1983) have shown that the presence of an inclusion could increase the magnitude of the adjacent stresses. Such defects are particularly damaging when they are close to the running surface (Miller et al., 1985). In addition, the residual tensile stress that exists at a level below the surface may have substantial influence on the initiation of a vertical defect. Figure 8 shows the Mode I stress intensity factor as a function of the crack length at the depth of $d_y = 17.78$ mm for various magnitudes of residual stress applied on the crack surface. The horizontal line represents the threshold stress intensity factor below which the defect is considered as being at the initiation stage. Clearly, the stress intensity factor can attain the threshold value for a relatively short crack length with residual stresses typical of rails in service. The
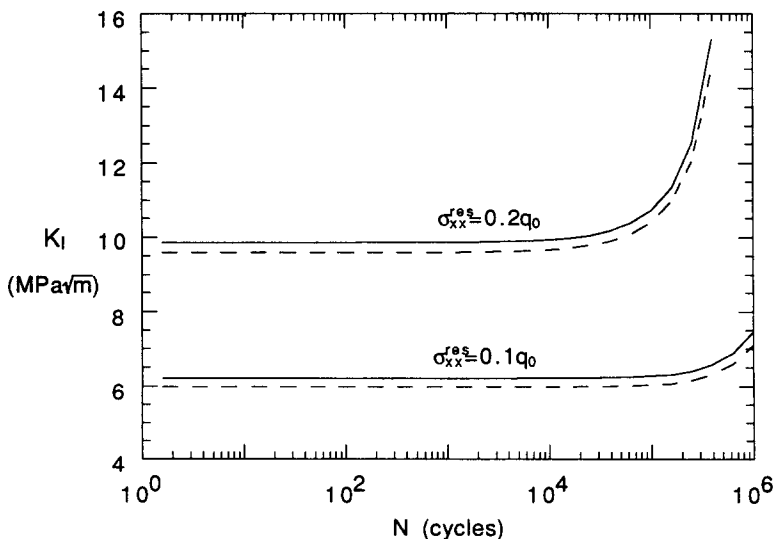

Fig. 10. Variation of mode I stress intensity factors, K_{IA} (solid) and K_{IB} (dash), as a function of loading cycle ($f = 0.1$, $e = 0$, $d_x = 0$ and $d_y = 17.78$ mm).

crack length as a function of number of loading cycles is shown in Fig. 9 for two values of residual stress. The fatigue crack growth is evaluated from the calculated stress intensity factor with the use of the Paris law. The initial crack length is $2c = 10.16$ mm and the center of the crack is originated at $d_y = 17.78$ mm. As the crack tip approaches the running surface or moves toward the head-web fillet, the growth of the crack is constrained by the compressive stresses. The analysis presented here indicates that growth at the upper crack tip stops at about 6.5 mm below the running surface in comparison with 6.35 mm observed from the fracture surface analysis. The variation of Mode I stress intensity factors during the fatigue life is shown in Fig. 10. The calculated stress intensity factors indicate that crack growth is faster at the upper crack tip than at the lower crack tip.

5. CONCLUSIONS

An idealized two-dimensional plane strain model is used to examine the fracture process of the vertical split head (VSH). It is shown that tensile stresses occur in most of the rail head due to shear friction on the contact surface and bending stresses as a result of eccentric wheel contact. However, the tensile stresses are relatively small compared with the maximum contact stress. Therefore, the vertical defect is more likely to be initiated by the influence of the residual tensile stresses upon an existing rail defect, such as an inclusion. As the crack length reaches a critical size, the residual stresses and tensile bending stresses provide the driving force for further crack growth. The growth of a fatigue crack in the vertical direction is evaluated from the calculated Mode I stress intensity factors with the use of the Paris law. In the propagation phase, the high magnitudes of compressive stresses that occur beneath the contact loading and the head-web juncture contribute to arrest growth of the vertical crack. A three-dimensional fracture analysis would be helpful to provide a more accurate assessment of such issues as longitudinal crack growth and cycles to failure.

REFERENCES

Barsom, J. M. and Imhof, E. J., Jr (1978). *Fatigue and Fracture Behavior of Carbon-Steel Rails.* ASTM STP644.
Erdogan, F., Gupta, G. D. and Cook, T. S. (1973). Numerical solution of singular integral equations. In *Methods of Analysis and Solutions of Crack Problems* (Edited by G. C. Sih). Noordhoff, Leyden.
Farris, T. N., Keer, L. M. and Steele, R. K. (1987). The effect of service loading on shell growth in rails. *J. Mech. Phys. Solids* 35(6), 677–700.
Hearle, A. D. and Johnson, K. L. (1985). Mode II stress intensity factors for a crack parallel to the surface of an elastic half-space subjected to a moving point load. *J. Mech. Phys. Solids* 33(1), 61–81.
Mayville, R. A. (1985). Metallurgical and fracture surface analysis of vertical split head defects. Report to Department of Transport.
Miller, G. R. and Keer, L. M. (1983). Interaction between a rigid indenter and a near-surface void or inclusion. *J. Appl. Mech.* 50, 615–620.
Miller, G. R. and Keer, L. M. (1985). A numerical technique for the solution of singular integral equations of the second kind. *Q. Appl. Math.* XLII(4), 455–465.
Miller, G. R., Keer, L. M. and Cheng, H. S. (1985). On the mechanics of fatigue crack growth due to contact loading. *Proc. Roy. Soc. Lond., Series A* 397, 197–209.
Muskhelishvili, N. I. (1953). *Singular Integral Equations* (English translation by J. M. R. Radok). Noordhoff, Groningen.
Orringer, O., Tang, Y. H., Gordon, J. E., Jeong, D. Y., Morris, J. M. and Perlman, A. B. (1988). Contact propagation life of detail fracture in rails. Report to Department of Transport.
Rice, J. R. (1988). Elastic fracture mechanics concepts for interfacial cracks. *J. Appl. Mech.* 55, 98–103.
Sheppard, S., Barber, J. R. and Comninou, M. (1985). Short subsurface cracks under conditions of slip and stick caused by a moving compressive load. *J. Appl. Mech.* 52, 811–817.

APPENDIX A

The kernels in eqns (28)–(30):

$$b_{11} = \frac{e^{-2h\eta}}{\Delta} \{[(2-y\eta)(1-e^{-2h\eta}) - 2h\eta(2-y\eta-3h\eta+2yh\eta^2)] e^{-y\eta} + [(2+y\eta)(1-e^{-2h\eta})$$

$$-2h\eta(2+y\eta-h\eta)] e^{y\eta}\}, \quad (A1)$$

$$b_{12} = \frac{e^{-2h\eta}}{\Delta}\{[(1-y\eta)(e^{-2h\eta}-1)-2h\eta(1-y\eta+3h\eta-2yh\eta^2)]e^{-y\eta}$$

$$+[(1+y\eta)(1-e^{-2h\eta})+2h\eta(1+y\eta-h\eta)]e^{y\eta}\}, \quad (A2)$$

$$b_{13} = \frac{e^{-h\eta}}{\Delta}\{[(2-y\eta)(e^{-2h\eta}-1)+h\eta(3-2y\eta+e^{-2h\eta})]e^{-y\eta}+[(2+y\eta)(e^{-2h\eta}-1)$$

$$+h\eta(5+2y\eta-8h\eta-4hy\eta^2+4h^2\eta^2-e^{-2h\eta})]e^{-(2h-y)\eta}\}, \quad (A3)$$

$$b_{14} = \frac{e^{-h\eta}}{\Delta}\{[(1-y\eta)(1-e^{-2h\eta})+h\eta(3-2y\eta-e^{-2h\eta})]e^{-y\eta}+[(1+y\eta)(e^{-2h\eta}-1)$$

$$-h\eta(1+2y\eta+4h\eta+4hy\eta^2-4h^2\eta^2+e^{-2h\eta})]e^{-(2h-y)\eta}\}, \quad (A4)$$

$$b_{21} = \frac{e^{-2h\eta}}{\Delta}\{[y\eta(1-e^{-2h\eta})-2h\eta(y\eta-h\eta-2yh\eta^2)]e^{-y\eta}+[y\eta(e^{-2h\eta}-1)+2h\eta(y\eta-h\eta)]e^{y\eta}\}, \quad (A5)$$

$$b_{22} = \frac{e^{-2h\eta}}{\Delta}\{[(1+y\eta)(e^{-2h\eta}-1)-2h\eta(1+y\eta+h\eta+2yh\eta^2)]e^{-y\eta}+[(1-y\eta)(1-e^{-2h\eta})$$

$$+2h\eta(1-y\eta+h\eta)]e^{y\eta}\}, \quad (A6)$$

$$b_{23} = \frac{e^{-h\eta}}{\Delta}\{[\eta(h-y)(1-e^{-2h\eta})+2yh\eta^2]e^{-y\eta}+[\eta(h-y)(e^{-2h\eta}-1)-2h\eta(y\eta-2yh\eta^2+2h^2\eta^2)]e^{-(2h-y)\eta}\},$$

$$\quad (A7)$$

$$b_{24} = \frac{e^{-h\eta}}{\Delta}\{[(1+y\eta)(1-e^{-2h\eta})+h\eta(1+2y\eta+e^{-2h\eta})]e^{-y\eta}+[(1-y\eta)(e^{-2h\eta}-1)$$

$$-h\eta(3-2y\eta+4h\eta-4hy\eta^2+4h^2\eta^2-e^{-2h\eta})]e^{-(2h-y)\eta}\}, \quad (A8)$$

$$b_{31} = \frac{e^{-2h\eta}}{\Delta}\{[(1-y\eta)(e^{-2h\eta}-1)+2h\eta(1-y\eta-h\eta+2yh\eta^2)]e^{-y\eta}$$

$$+[(1+y\eta)(1-e^{-2h\eta})-2h\eta(1+y\eta-h\eta)]e^{y\eta}\}, \quad (A9)$$

$$b_{32} = \frac{e^{-2h\eta}}{\Delta}\{[y\eta(1-e^{-2h\eta})+2h\eta(y\eta-h\eta+2yh\eta^2)]e^{-y\eta}+[y\eta(e^{-2h\eta}-1)-2h\eta(y\eta-h\eta)]e^{y\eta}\}, \quad (A10)$$

$$b_{33} = \frac{e^{-h\eta}}{\Delta}\{[(1-y\eta)(1-e^{-2h\eta})-h\eta(1-2y\eta+e^{-2h\eta})]e^{-y\eta}+[(1+y\eta)(e^{-2h\eta}-1)$$

$$+h\eta(3+2y\eta-4h\eta-4hy\eta^2+4h^2\eta^2-e^{-2h\eta})]e^{-(2h-y)\eta}\}, \quad (A11)$$

$$b_{34} = \frac{e^{-h\eta}}{\Delta}\{[\eta(h-y)(1-e^{-2h\eta})-2yh\eta^2]e^{-y\eta}+[\eta(h-y)(e^{-2h\eta}-1)+2h\eta(y\eta+2yh\eta^2-2h^2\eta^2)]e^{-(2h-y)\eta}\}.$$

$$\quad (A12)$$

APPENDIX B

The elastic field in an infinite plane due to the edge dislocations distributed along $x = d_x$ and $|y-d_y| \leqslant c$:

$$2\mu\frac{\partial u_x}{\partial x} = \frac{\mu}{\pi(\kappa+1)}\int_{d_y-c}^{d_y+c}\left\{\frac{y-t}{r^2}\left[(\kappa-1)+\frac{4(x-d_x)^2}{r^2}\right]b_x(t)+\frac{x-d_x}{r^2}\left[(1-\kappa)+\frac{4(y-t)^2}{r^2}\right]b_y(t)\right\}dt, \quad (B1)$$

$$2\mu\frac{\partial u_y}{\partial x} = \frac{\mu}{\pi(\kappa+1)}\int_{d_y-c}^{d_y+c}\left\{\frac{x-d_x}{r^2}\left[(\kappa-1)+\frac{4(y-t)^2}{r^2}\right]b_x(t)+\frac{y-t}{r^2}\left[(\kappa-1)+\frac{4(y-t)^2}{r^2}\right]b_y(t)\right\}dt, \quad (B2)$$

$$\sigma_{xx} = \frac{2\mu}{\pi(\kappa+1)}\int_{d_y-c}^{d_y+c}\left\{\frac{y-t}{r^2}\left[1+\frac{2(x-d_x)^2}{r^2}\right]b_x(t)-\frac{x-d_x}{r^2}\left[1-\frac{2(y-t)^2}{r^2}\right]b_y(t)\right\}dt, \quad (B3)$$

$$\sigma_{yy} = \frac{2\mu}{\pi(\kappa+1)}\int_{d_y-c}^{d_y+c}\left\{\frac{y-t}{r^2}\left[1-\frac{2(x-d_x)^2}{r^2}\right]b_x(t)-\frac{x-d_x}{r^2}\left[1+\frac{2(y-t)^2}{r^2}\right]b_y(t)\right\}dt, \quad (B4)$$

$$\sigma_{xy} = \frac{2\mu}{\pi(\kappa+1)}\int_{d_y-c}^{d_y+c}\left\{\frac{x-d_x}{r^2}\left[-1+\frac{2(y-t)^2}{r^2}\right]b_x(t)+\frac{y-t}{r^2}\left[1-\frac{2(x-d_x)^2}{r^2}\right]b_y(t)\right\}dt, \quad (B5)$$

where

C. H. Kuo *et al.*

$$r^2 = (x-d_x)^2 + (y-t)^2. \tag{B6}$$

APPENDIX C

The kernels in eqns (38)–(41):

$$k_{11} = -\int_0^\infty \frac{a_{13}}{\Delta} \sin \eta(x-t)\, d\eta, \tag{C1}$$

$$k_{12} = -k_{21} = \int_0^\infty \frac{1}{\Delta} [a_{14} \cos \eta(x-t) + 2(\kappa+1)h^2\eta^2\, e^{-2h\eta}]\, d\eta, \tag{C2}$$

$$k_{13} = \frac{-2\mu}{(\kappa+1)} \int_0^\infty \frac{1}{\Delta} \{[(a_{11}-a_{12})s\eta - a_{11}]\, e^{-s\eta} + [(a_{13}+a_{14})(h-s)\eta - a_{13}]\, e^{-(h-s)\eta}\} \cos \eta(x-d_x)\, d\eta$$
$$+ 4\mu \frac{(x-d_x)^2(h-s)}{r^4}, \tag{C3}$$

$$k_{14} = \frac{-2\mu}{(\kappa+1)} \int_0^\infty \frac{1}{\Delta} \{[(a_{11}-a_{12})s\eta - a_{12}]\, e^{-s\eta} - [(a_{13}+a_{14})(h-s)\eta + a_{14}]\, e^{-(h-s)\eta}\} \sin \eta(x-d_x)\, d\eta$$
$$+ 4\mu \frac{(x-d_x)(h-s)^2}{r^4}, \tag{C4}$$

$$k_{22} = \int_0^\infty \frac{1}{\Delta} [-a_{24} \sin \eta(x-t) - 4(\kappa+1)h(x-t)\eta^2\, e^{-2h\eta}]\, d\eta, \tag{C5}$$

$$k_{23} = \frac{-2\mu}{(\kappa+1)} \int_0^\infty \frac{1}{\Delta} \{[(a_{21}+a_{22})s\eta - a_{21}]\, e^{-s\eta} + [(a_{23}-a_{24})(h-s)\eta - a_{23}]\, e^{-(h-s)\eta}\} \sin \eta(x-d_x)\, d\eta$$
$$+ 4\mu \frac{(x-d_x)(h-s)^2}{r^4}, \tag{C6}$$

$$k_{24} = \frac{-2\mu}{(\kappa+1)} \int_0^\infty \frac{1}{\Delta} \{-[(a_{21}+a_{22})s\eta + a_{22}]\, e^{-s\eta} + [(a_{23}-a_{24})(h-s)\eta - a_{24}]\, e^{-(h-s)\eta}\} \cos \eta(x-d_x)\, d\eta$$
$$+ 4\mu \frac{(h-s)^3}{r^4}, \tag{C7}$$

$$k_{31} = \int_0^\infty \frac{-b_{13}}{\Delta} \sin \eta(d_x-t)\, d\eta + \int_0^\infty [-2+(h-y)\eta]\, e^{-(h-y)\eta} \sin \eta(d_x-t)\, d\eta, \tag{C8}$$

$$k_{32} = \int_0^\infty \frac{1}{\Delta} \{b_{14} + 8h(2y-h)\eta^2\, e^{-2h\eta} + [1-(h-y)\eta]\, e^{-(h-y)\eta}\} \cos \eta(d_x-t)\, d\eta, \tag{C9}$$

$$k_{33} = \frac{-2\mu}{(\kappa+1)} \int_0^\infty \frac{1}{\Delta} \{[(b_{11}-b_{12})s\eta - b_{11}]\, e^{-s\eta} + [(b_{13}+b_{14})(h-s)\eta - b_{13}]\, e^{-(h-s)\eta}\}\, d\eta$$
$$- \frac{2\mu}{(\kappa+1)} \int_0^\infty \{[2-(3s+y)\eta + 2ys\eta^2]\, e^{-(y+s)\eta} - [2-(4h-y-3s)\eta + 2(h-y)(h-s)\eta^2]\, e^{-(2h-y-s)\eta}\}\, d\eta, \tag{C10}$$

$$k_{41} = \int_0^\infty \left\{ \frac{b_{33}}{\Delta} + [1-(h-y)\eta]\, e^{-(h-y)\eta} \right\} \cos \eta(d_x-t)\, d\eta, \tag{C11}$$

$$k_{42} = \int_0^\infty \left[\frac{-b_{34}}{\Delta} - (h-y)\eta\, e^{-(h-y)\eta} \right] \sin \eta(d_x-t)\, d\eta, \tag{C12}$$

$$k_{44} = \frac{-2\mu}{(\kappa+1)} \int_0^\infty \frac{1}{\Delta} \{-[(b_{31}+b_{32})s\eta + b_{32}]\, e^{-s\eta} + [(b_{33}-b_{34})(h-s)\eta - b_{34}]\, e^{-(h-s)\eta}\}\, d\eta$$
$$- \frac{2\mu}{(\kappa+1)} \int_0^\infty \{[(y-s)\eta + 2ys\eta^2]\, e^{-(y+s)\eta} + [(y-s)\eta - 2(h-y)(h-s)\eta^2]\, e^{-(2h-y-s)\eta}\}\, d\eta, \tag{C13}$$

$$p_1 = \int_0^\infty \frac{1}{\Delta} \left\{ \frac{\pi}{\eta} J_1(\eta a)[-fa_{11} \sin \eta(x-e) + a_{12} \cos \eta(x-e)] - \pi a(\kappa+1)h^2\eta^2\, e^{-2h\eta} \right\} d\eta, \tag{C14}$$

$$p_2 = \int_0^\infty \frac{1}{\Delta} \left\{ \frac{\pi}{\eta} J_1(\eta a)[f a_{12} \cos \eta(x-e) - a_{22} \sin \eta(x-e)] - \pi a(\kappa+1) h \eta [f h \eta - 2(x-e)\eta] e^{-2h\eta} \right\} d\eta, \quad \text{(C15)}$$

$$p_3 = \int_0^\infty \frac{\pi}{\eta} J_1(\eta a) \left\{ f\left[(2-y\eta) e^{-y\eta} - \frac{b_{11}}{\Delta} \right] \sin \eta(d_x-e) + \left[(1-y\eta) e^{-y\eta} + \frac{b_{12}}{\Delta} \right. \right.$$
$$\left. \left. - \frac{8h(2y-h)\eta^2 e^{-2h\eta}}{\Delta} \right] \cos \eta(d_x-e) \right\} d\eta, \quad \text{(C16)}$$

$$p_4 = \int_0^\infty \frac{\pi}{\eta} J_1(\eta a) \left\{ f\left[(1-y\eta) e^{-y\eta} + \frac{b_{31}}{\Delta} \right] \cos \eta(d_x-e) + \left[y\eta\, e^{-y\eta} - \frac{b_{32}}{\Delta} \right] \sin \eta(d_x-e) \right\} d\eta, \quad \text{(C17)}$$

where

$$a_{11} = (\kappa+1) e^{-h\eta}[1 - h\eta - (1+h\eta) e^{-2h\eta}], \quad \text{(C18)}$$

$$a_{12} = a_{12} = (\kappa+1) h\eta\, e^{-h\eta} (1 - e^{-2h\eta}), \quad \text{(C19)}$$

$$a_{13} = (\kappa+1) e^{-2h\eta} (-1 + 2h\eta - 2h^2\eta^2 + e^{-2h\eta}), \quad \text{(C20)}$$

$$a_{23} = -a_{14} = 2(\kappa+1) h^2\eta^2 e^{-2h\eta}, \quad \text{(C21)}$$

$$a_{22} = (\kappa+1) e^{-h\eta} [1 + h\eta - e^{-2h\eta}(1 - e^{-2h\eta})], \quad \text{(C22)}$$

$$a_{24} = (\kappa+1) e^{-2h\eta} (-1 - 2h\eta - 2h^2\eta^2 + e^{-2h\eta}), \quad \text{(C23)}$$

and b_{ij}, $i = 1, 3$, $j = 1, 4$ are the same as those listed in Appendix A.